Title
Numerical and Flow Sensitivity Study of Propeller and Wing Interaction Noise

Journal
Vertical Flight Society 80th Annual Forum and Technology Display

Authors
Trembois, N
Brown, E
Lee, S
et al.

Publication Date
2024

Numerical and Flow Sensitivity Study of Propeller and Wing Interaction Noise

Nikos Trembois
PhD Student

Ethan Brown
PhD Student

Seongkyu Lee
Professor

University of California, Davis
Davis, California, USA

Kenneth S. Brentner
Professor Pennsylvania State University
University Park, Pennsylvania, USA

ABSTRACT

High-fidelity simulations are used to enhance the understanding of the sensitivity of propeller-wing interactions across a spectrum of conditions, focusing on both aerodynamics and aeroacoustics. The aerodynamics is analyzed using high-fidelity computational fluid dynamics, while the acoustics is assessed through the application of impermeable Ffowcs Williams and Hawkings surfaces. Initial assessments concentrate on the influence of simulation parameters on both convergence and accuracy of numerical results. It is determined that reducing the wake grid spacing from 10% of the reference chord length to 7.5% offers no notable improvement to acoustic predictions. Moreover, comparisons between acoustic predictions employing the SST turbulence model and the SA model, with and without transition modeling, reveals differences that are minor in comparison to the prediction errors observed against experimental data. Then, the sensitivities of both aerodynamic and aeroacoustic responses are examined in relation to freestream and tip Mach numbers, angle of attack, and side slip angle. Aerodynamic analyses highlight a strong dependency of both steady and unsteady propeller loading on freestream and tip Mach numbers, and the wing angle of attack. The wing steady loading demonstrates sensitivity primarily to freestream Mach number and the wing angle of attack, whereas the unsteady wing loading is influenced by freestream and tip Mach numbers, and the angles of attack of both the propeller and the wing. The introduction of a side slip angle is found to alter propeller and wing interactions significantly, leading to an increase in propeller thrust. Aeroacoustic investigations show that the sound pressure level of the first blade passing frequency of the propeller rises with tip Mach number but decreases as the freestream Mach number increases. Wing noise exhibits increased sensitivity to tip Mach number with rising freestream Mach number. However, due to phasing, it is not always possible to distinctly separate trends in total noise from the underlying physical mechanisms such as the destructive interference occurring between propeller and wing noise signals. Additionally, the side slip angle is found to amplify the propeller, wing, and the system noise as a whole.

INTRODUCTION

Recent developments in advanced air mobility (AAM) have resulted in the emergence of aircraft designs characterized by complex flow interactions. Specifically, AAM vehicles often feature tiltrotors that transition from hover to edgewise to axial flight, leading to drastically varying flow interaction characteristics throughout the flight envelope. The unsteady aerodynamic loading associated with these varying flow conditions become significant sources of noise.

Computational and experimental methods have been employed to enhance our understanding of the aerodynamics and aeroacoustics in propeller and wing interactions across various test models. Lim (Ref. 1) provided detailed insights into the aerodynamic interactions between a wingtip-mounted XV-15 rotor and a NACA 0023 airfoil wing through high-fidelity computational fluid dynamics (CFD), highlighting the impact of wing thickness and loading on propeller aerodynamics. Zhang et al. (Ref. 2) underscored the significance of impact of flow interactions from wingtip-mounted propellers on the noise using medium-fidelity vortex methods, noting a noise increase of up to 10 dB when including propeller and wing aerodynamic interactions. Stephenson et al. (Ref. 3) investigated the acoustics of a wing and pusher rotorprop in a wind tunnel with both full and half-span wings to represent inboard and tip-mounted rotorprop configurations, respectively, identifying a notable noise increase due to the interaction between wing wake flows and propeller blades. Jia et al. (Ref. 4) applied high-fidelity CFD to predict noise from these tests, achieving good agreement between numerical simulations and experimental data. Zawodny et al. (Ref. 5) examined how wing's horizontal and vertical positions affects propeller-wing interactional noise, concentrating on the first blade passing frequency and demonstrating the influence of wing loading

Presented at the Vertical Flight Society 80th Annual Forum & Technology Display, Montréal, Québec, Canada, May 7–9, 2024.

on both noise amplitude and directivity. More recently, Trembois et al. (Ref. 6) validated computational methods against these experimental results (Ref. 5) for predicting propeller and wing tonal noise using high-fidelity CFD, showing good agreement between numerical predictions and experimental data regarding noise amplitude and directivity. Ramsarran et al. (Ref. 7) conducted a similar noise validation study using a medium-fidelity vortex particle method. While the prediction of isolated propeller noise was comparable with CFD results, accurately capturing the wing interaction noise proved to be challenging with the medium-fidelity model.

As described in the previous paragraph, a vast body of research has been dedicated to exploring the sound source and propagation for aircraft equipped with propeller and wing configurations, covering a wide range of designs. Despite this, the influence of flow speeds, direction, and propeller thrust on aerodynamic and acoustic interactions has not been as extensively examined. Aircraft capable of transitioning between flight modes require a comprehensive understanding of how unsteady aerodynamic and acoustic interactions occur across different flow velocities and angles. Notably, Draper et al. (Ref. 8) delved into the aerodynamic performance of a tiltrotor under various thrust levels and flow conditions through wind tunnel experiments. However, their research only focused on the aerodynamic performance without involving acoustic analysis. Quackenbush et al. (Ref. 9) validated the predictions of aerodynamic performance using a panel-based vortex method for these experimental cases. Brown et al. (Ref. 10) includes preliminary aeroacoustic results of these experimental cases for different flow conditions with a wing flap being employed.

This paper aims to present an in-depth investigation of the aerodynamics and aeroacoustics of a propeller and wing under various flow conditions, utilizing high-fidelity computational methods. The earlier high-fidelity CFD simulations adhered to established best practices for rotorcraft simulations (Refs. 11–14), including aspects like grid resolution, turbulence modeling, and temporal resolution, etc. This paper further explores these numerical parameters to determine their impact on acoustic outcomes for the specific configuration of interest. The research also assesses the acoustic sensitivity to changes in flow conditions while unraveling the complexities of aerodynamic interactions. The study will concentrate on a propeller paired with an aft-mounted wing, following the experimental setup by Zawodny et al. (Ref. 5), and will examine a wide spectrum of flow conditions. These variations will encompass changes in freestream velocity, angle of attack, propeller rotation rate, and side slip angle, offering a spectrum of advance ratios and wing lift coefficients to assess the relative impact of various interaction effects. It should be noted that this paper exclusively addresses tonal noise, acknowledging that broadband noise might also be significant for this setup. The exploration of broadband noise is reserved for future research, employing more sophisticated analytical and numerical tools (Refs. 15, 16).

METHODS

This paper conducts a comprehensive analysis of the flow field and aerodynamic performance using CFD simulations. Aeroacoustic predictions are subsequently made based on the surface pressure data. To ensure precise surface modeling, the simulations employ curvilinear overset grids. The creation of near-body grids is facilitated by the use of Chimera Grid Tools (CGT) and OVERGRID, whereas off-body grids are generated using OVERFLOW. The scope of this research includes examining variations in both numerical and flow parameters. An initial study of simulation parameters aims to find an optimal balance between the efficiency and accuracy of the simulation. This effort is followed by an in-depth investigation of flow parameters, which is a main topic of this paper.

Grids

The Outer Mold Line (OML) is defined using a hundred section profiles of the Mejzlik propeller blade, evenly distributed from the root to the tip. UCD-BladeGen (Ref. 17) generates the surface grids from the OML utilizing Chimera Grid Tools (CGT). The propeller blades are meshed with structured O-Type grids with an equal number of grid points being placed on both the suction and pressure sides of the blade. The holes at the root and the tip of the blade grid are sealed with a collar grid that connects to the nacelle and a cap grid, respectively. Cartesian off-body grids are dynamically created by OVERFLOW at runtime.

The blade surface grids are generated with 125 chordwise points on each of the suction and pressure sides. The blunt trailing edge is resolved with fourteen grid points. The grid spacing at the leading edge is set to 0.05% of the local chord, while the trailing edge grid spacing is even finer at 0.02% of the local chord, allowing for precise simulation of flow separation and wake flows. To accurately model the spanwise variation, the model incorporates 150 spanwise grid points, with a spacing of 0.1% of the reference chord, which is defined later, at the root and the tip.

The volume structured grids extend one reference chord length into the flow, as shown in Fig. 1. The reference chord, denoted as C_{ref} , is defined at 75% of the blade radius, with a value of 0.1 ft. The initial volume spacing is set at 7×10^{-6} ft to ensure $y+ \leq 1$. The finest off-body grid spacing (level-1) is established based on the spacing at the edge of the near-body grids. The grid spacing increases through eight levels of Cartesian grids until it meets the freestream boundary condition, which is located 10 propeller radii (6.56 ft) away from the propeller center. This meticulous grid strategy results in a comprehensive mesh comprising 25M near-body grid points and 22M off-body grid points, totaling 47M points. Figure 2 shows the near- and off-body grids for the propeller blade, nacelle, and wing.

Two variations of volume grids are generated to assess the impact of grid resolution on the accuracy of aeroacoustic predictions. The number of volumetric points in the near-body grids and the spacing at the edge of these grids are adjusted

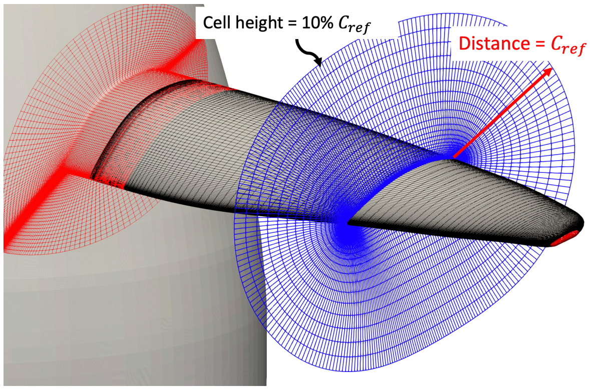

Fig. 1: The baseline surface and near-body volume grids for the propeller blade

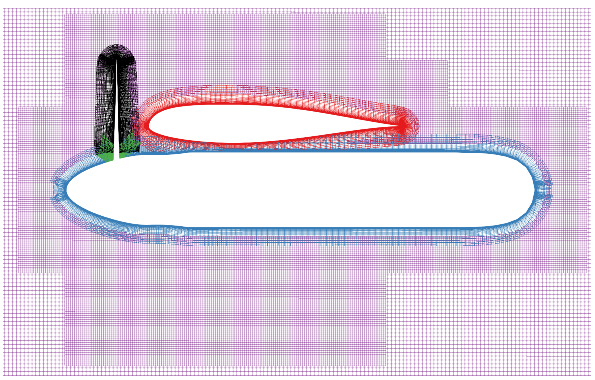

Fig. 2: Near- and off-body grid spacing and domain for the baseline grid for the propeller, nacelle and wing.

between configurations. The fine grids feature 165 points in the wall-normal direction, while the coarse grid includes 65 points. Additionally, the spacing at the edge of the near-body grids is set at 7.5% of C_{ref} for the fine grids and 10% of C_{ref} for the coarse grids. For more detailed information on the grid generation process, refer to Ref. 6.

Simulation

NASA's OVERFLOW (Refs. 18, 19) is utilized to simulate the flow, solving the unsteady compressible Reynolds Averaged Navier-Stokes (RANS) equations. The $k-\omega$ and Spalart-Allmaras (SA) and the Shear Stress Transport (SST) turbulence models, supplemented by the delayed detached eddy simulation (DDES) approach, are employed to accurately capture the complex vortical eddies in the wake region. For the simulation, the propeller blades are advanced by 0.25 azimuthal degrees per time step, necessitating 1440 physical time steps per revolution. A dual-time stepping strategy is implemented, with a residual cap set to two orders of magnitude. The temporal numerical scheme leverages second-order backward differencing, while a fifth-order central spatial scheme is used for inviscid flux terms. The baseline conditions are set with a freestream Mach number of 0.068 and a tip Mach number of 0.361, corresponding to 6000 RPM.

The steady and unsteady wing pressure coefficient is calculated along the chord at four spanwise locations as shown in Fig. 3. The steady pressure is determined within the propeller wake, 0.5 propeller radii on either side of the propeller's axis of rotation. These two locations are referred to as the advancing and retreating sides. On the advancing side, the propeller blade moves past the wing from the pressure to the suction side, whereas, on the retreating side, the blade transitions from the suction side back to the pressure side. The root-mean-square (RMS) of the pressure coefficient is calculated at two specific locations: directly on the propeller centerline and 0.866 propeller radii from the centerline on the advancing blade side. These locations are identified as the centerline and the advancing side, respectively. The distinction between the two locations on the advancing side is made based on the pressure metric, with the measurement location for the RMS of pressure strategically positioned to align with the propeller tip vortex.

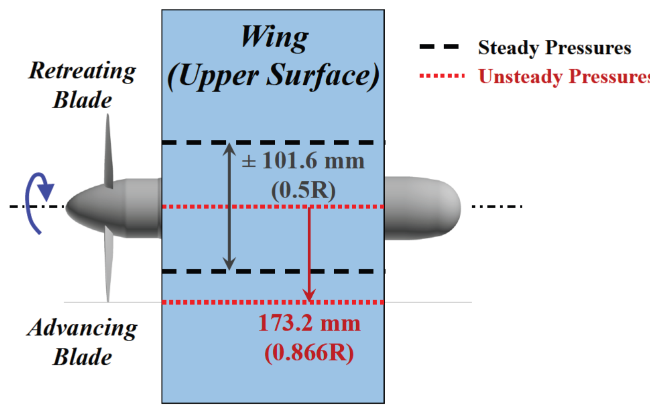

Fig. 3: The pressure measurement locations on the wing for steady pressure (C_p) and unsteady pressure ($C'_{p,\,RMS}$) (Ref. 5).

The wing leading edge is located 0.25 propeller radii behind the propeller disk and 0.5 propeller radii above the propeller centerline. The angle of attack for both the propeller and the wing is increased by five degrees, either independently or simultaneously, as shown in Fig. 5. For the propeller alone, a five degree angle of attack is added to the propeller where the center of rotation intersects the propeller plane. For the wing, the angle of attack is adjusted around the eighth-chord position. When both the propeller and the wing are simulated with an increased angle of attack, the center of rotation is positioned 47.5 inches behind the propeller disk plane along the propeller's axis of rotation. The side slip (β) angle is established in a manner that positive angles direct airflow toward the port side of the wing. The side slip angle and propeller rotation direction are illustrated in Fig. 4.

Aeroacoustics

The thickness and loading noise are computed utilizing PSU-WOPWOP (Refs. 20–23) based on the surface motion and surface pressure data, respectively. An impermeable Ffowcs Williams and Hawkings (FW-H) surface (Ref. 24) is used for

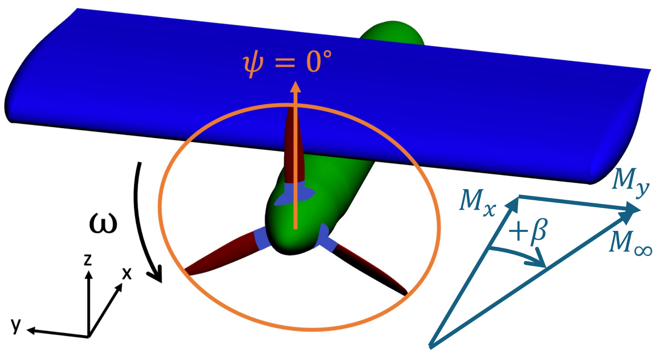

Fig. 4: Illustration of propeller rotation direction and side slip angle.

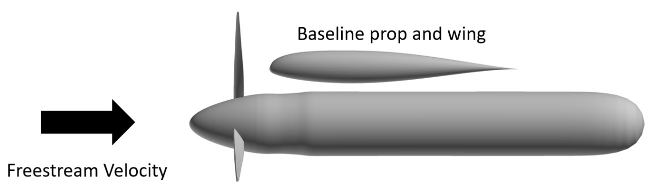

(a) Setup for the $\boldsymbol{\Delta X/R = 0.25,\ \Delta Z/R = 0.5}$ wing position with no angle of attack.

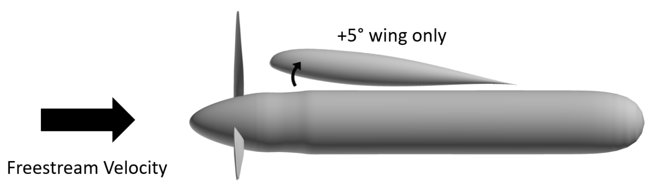

(b) Setup for the $\boldsymbol{\Delta X/R = 0.25,\ \Delta Z/R = 0.5}$ wing position, for the +5° wing angle.

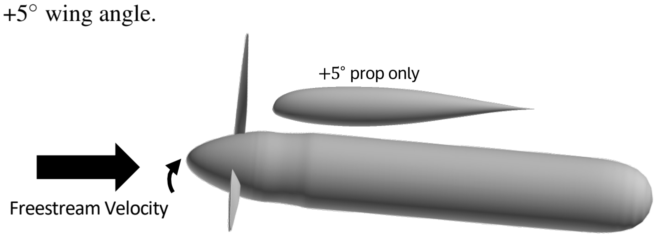

(c) Setup for the $\boldsymbol{\Delta X/R = 0.25,\ \Delta Z/R = 0.5}$ wing position, for the +5° propeller angle.

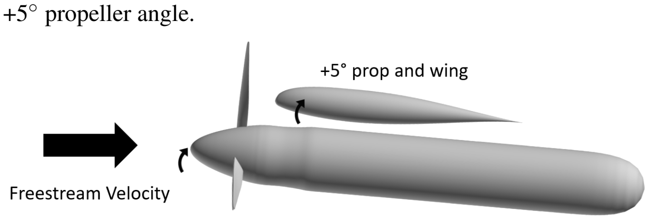

(d) Setup for the $\boldsymbol{\Delta X/R = 0.25,\ \Delta Z/R = 0.5}$ wing position, for the +5° propeller and wing angle.

Fig. 5: Geometry of propeller and wing for various angle of attack configurations.

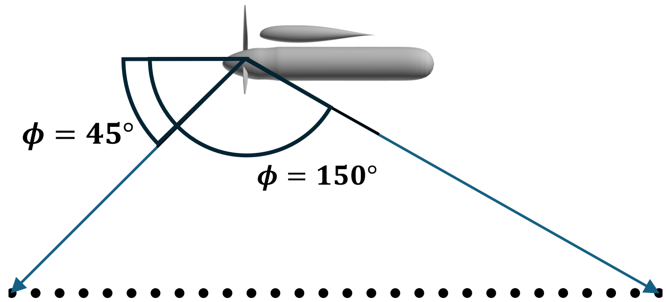

Fig. 6: Axial positions and elevations angles of the linear array of observers.

each propeller blade and the wing to facilitate these calculations. For the blade, the FW-H surface modeling incorporates the O-type blade grid and the tip cap, while deliberately excluding the collar grid to focus the analysis on the most critical noise-generating elements. On the other hand, the wing's FW-H surface modeling includes the O-type wing grid and both cap grids, ensuring a comprehensive acoustic analysis of the wing structure. PSU-WOPWOP calculates acoustic pressure using Farassat Formulation 1A (Ref. 25), an integral solution to the FW-H equation (Ref. 24).

The acoustic pressure predictions are conducted using a linear array of 28 equally spaced observers, as depicted in Fig. 6. This array is strategically positioned 11.5 feet below the propeller's centerline, at a lateral angle of 50°, and is aligned parallel to the freestream direction to accurately capture the acoustic emissions. The proximity of the linear array to the source of the noise, the propeller and wing, is maintained at a minimum distance of 13.7 feet, equivalent to 20 propeller radii. The array spans an elevation angle range from 45° to 150°, effectively covering a substantial arc around the propeller disk. This encompasses a distance of 8.8 feet in front of the propeller disk and extends to 15.2 feet behind it.

RESULTS

Numerical Parameter Study

Convergence with Rotor Revolution The acoustic pressure is evaluated from the average loading at two distinct revolutions to assess the convergence of the acoustic results. The acoustic pressure is calculated from the surface pressure at both the 6th and 8th revolutions, as presented in Fig. 7. The maximum discrepancy in acoustic pressure prediction is 0.067 dB at $\phi = 135°$. For more information on the behavior of the predicted noise at high elevation angles, specifically near $\phi = 135°$, see the Appendix. The difference in acoustic magnitude between the 6th and 8th revolutions is consistently less than one-tenth of the predictive error when compared to experimental results (Ref. 5) across all elevation angles. Consequently, all remaining simulations use six propeller revolutions to ensure temporal convergence. The decision for the convergence at the 6th revolution was initially made by aerodynamic convergence (Ref. 6) and is now corroborated for acoustic convergence.

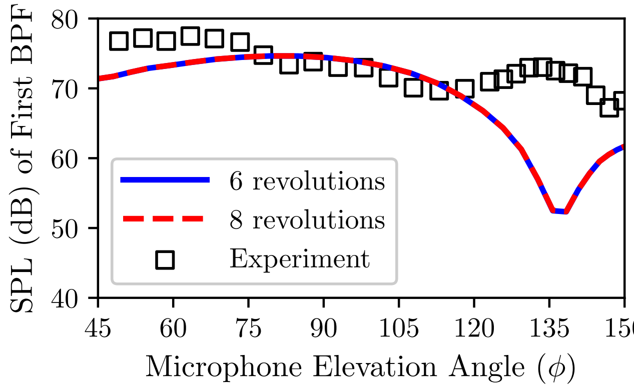

Fig. 7: A comparison of the directivity between the 6th and 8th propeller revolution with respect to the experimental measurements.

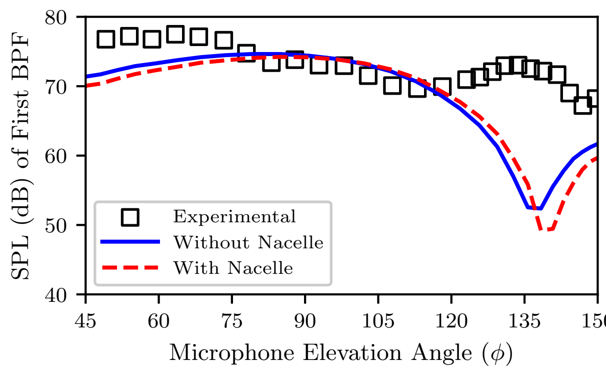

Fig. 8: A comparison of the directivity with and without the nacelle grid included with respect to the experimental measurements.

Effect of Nacelle The acoustic pressure is assessed both with and without the nacelle surface to determine the significance of the nacelle on the directivity of the first BPF. These results are compared with experimental data (Ref. 5), as depicted in Figure 8. For elevation angles up to $\phi = 130°$, the maximum deviation between the acoustic results with and without the nacelle is only 1.41 dB. The predictions diverge more significantly at high elevation angles where the predictions noticeably differ from the experimental outcomes. The largest difference in SPL for the first BPF is observed at $\phi = 138°$, amounting to a magnitude of 3.15 dB. In the range of $\phi = 75°$ to $\phi = 120°$, where the prediction error remains below 1% compared to the experimental data, both prediction methodologies also exhibit a difference of less than 1%. Hence, including the nacelle in the acoustic simulation has a minimal impact. Given these findings, the nacelle is excluded from the impermeable FW-H surface in subsequent acoustic predictions.

Effect of Grid Resolution Figure 9 presents a comparison of the directivity between the coarse and fine grid. The largest discrepancy between the coarse and fine grid at elevation angles less than 120° is 0.73 dB. However, the predictions diverge for observers further aft of the propeller. Nonetheless, both simulations deviate from the experimental data by over 5.0 dB at those observers, equivalent to a 7.4% error. The fine grid does not demonstrate a discernible advantage. Given that the disparities are minimal where the prediction is deemed reliable, the additional computational expense of employing the fine grid cannot be justified. In the subsequent analysis, the coarse or baseline grid is used.

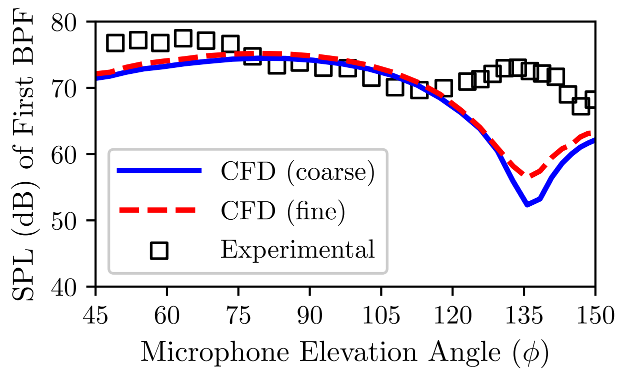

Fig. 9: A comparison of the directivity between the coarse and fine volume grids with respect to the experimental measurements.

Effect of Turbulence Model Two turbulence models are evaluated: the SA model and the Shear Stress Transport (SST) formulation of the $\mathrm{k}-\omega$ model. The SA model is simulated with and without the Coder transition model. DDES is utilized across all three turbulence models. Figure 10 compares the average and RMS of the pressure coefficient at four sections of the wing during one rotor revolution. The average pressure over the wing is not sensitive to the turbulence model on either the advancing or retreating side. There are discrepancies in the prediction of the pressure RMS between the turbulent models, in particular near the leading edge. Along the tip vortex trajectory, the SA models predicts 11% higher $C'_{\mathrm{p, RMS}}$ than the SST model at 0.14 x/c on the pressure side. The SA model predicts by 9.3% higher unsteady pressure than the SST model on the propeller centerline at 0.05 x/c. In this plot, the predicted results are also compared with the experimental data. Overall, the prediction matches very well with the experimental data for both averaged and RMS of the pressure coefficient.

Figure 11 contrasts the acoustic directivity of the three turbulence models against wind tunnel measurements. The maximum discrepancy between the SA and SST models is 0.96 dB. Throughout all elevation angles, the SA transition model remains within 0.85 dB of the SA model. Since the deviation in aeroacoustic predictions is less than 1 dB, and the computational time between the SST and SA models is found to be indistinguishable for this model, the SST fully turbulent model is used for the remaining of this paper.

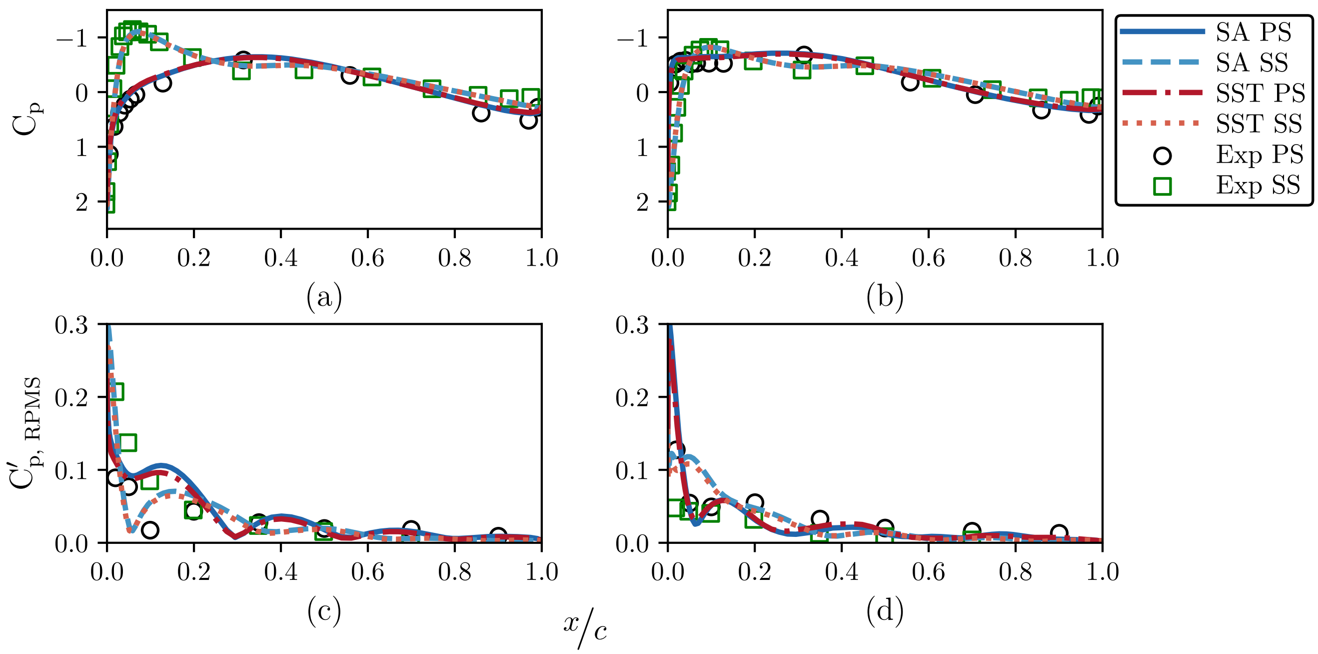

Fig. 10: Comparison of predicted wing pressure with SA and SST turbulence models: (a) average pressure coefficient on the advancing side, (b) average pressure coefficient on the retreating side, (c) RMS of pressure coefficient on advancing side, and (d) RMS of pressure coefficient on the centerline.

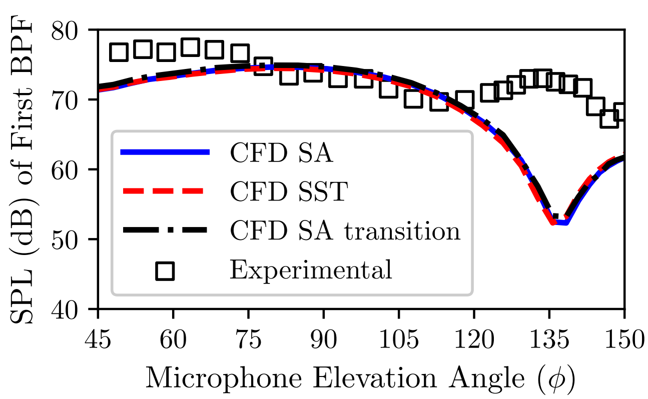

Fig. 11: Acoustic directivity of three turbulence models compared to experimental measurements.

Flow Parameter Study

Freestream and Tip Velocity In this study, the propeller rotation rate, expressed as tip Mach number, and the freestream velocity are varied to assess their impact on aerodynamic performance and noise. Changes in the freestream and rotational speeds affect both the average thrust coefficient and the load distribution on the propeller. The thrust coefficient of the propeller is defined as $C_T = T/\rho_\infty n^2 D_p^4$, where n represents the propeller's rotations per second and D_p is its diameter. The simulations maintain constant atmospheric flow properties, specifically density, ensuring that the thrust coefficient's variation is primarily influenced by changes in the tip Mach number and thrust. The number of revolutions required to achieve periodic convergence is consistent across the different flow conditions, indicating that the variations in speeds does not affect the convergence criteria for these simulations. It is worthwhile noting that we do not consider the trim conditions for these various conditions. In other words, the pitch is constant for all the cases.

Two sets of simulations with varying flow speeds are defined relative to the nominal condition (M_{tip} = 0.361 and M_∞ = 0.068). The initial set roughly halves and doubles the nominal freestream and tip Mach numbers, creating 9 simulations defined by all unique combinations of three freestream and tip Mach numbers (M_∞ = 0.03, 0.068, 0.15 and M_{tip} = 0.18, 0.361, 0.5), henceforth, referred to as the basic set of flow conditions. After examining the outcomes at the boundaries of the basic flow conditions, a second set of flow conditions is determined to closely analyze trends near the nominal condition. These conditions vary from 0.25 to 0.4 for tip Mach numbers and from 0.05 to 0.09 for freestream Mach numbers, including the nominal condition. The result is a matrix of three freestream Mach numbers (0.05, 0.068, and 0.09) and four tip Mach numbers (0.25, 0.3, 0.361, 0.4), referred to as the refined set of flow conditions.

Aerodynamic Results

Basic Flow Conditions Within the coarse set of flow conditions, the thrust coefficient consistently increases with RPM at a fixed airspeed as depicted in Fig. 12. This average thrust

Table 1: The average thrust coefficient over one revolution for each flow condition in the coarse set.

M_{tip} \ M_∞	0.03	0.068	0.15
0.18	0.0254	−0.0100	N/A
0.361	0.145	0.0945	−0.0513
0.50	0.275	0.240	0.413

coefficient is summarized in Table 1. Conversely, an increase in freestream velocity at a fixed RPM leads to a decrease in the propeller thrust coefficient. At the baseline rotation rate (M_{tip} = 0.361), the highest freestream velocity (M_∞ = 0.15) results in negative thrust due to the large advance ratio, causing negative angles of attack on the propeller blades. At the lowest RPM and highest freestream velocity, the conditions become unstable, leading to issues with the simulation's convergence. Consequently, the data for the coarse set of conditions encompasses only 8 flow scenarios. With an increase in freestream velocity, the influence of wing loading on the propeller thrust becomes more pronounced, resulting in an enhanced thrust fluctuation magnitude. Additionally, though more subtly, the periodic thrust magnitude also increases with rising RPM for a given airspeed.

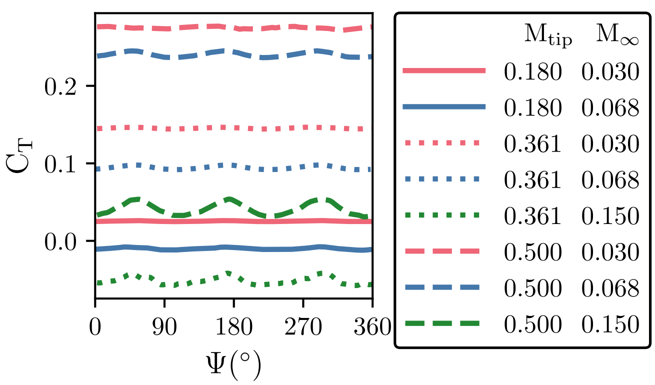

Fig. 12: Converged thrust coefficient for flow conditions over one revolution.

Figure 13 illustrates the thrust distribution at $r = 0.75R$ on a single blade during its final revolution. For the same M_∞ values, the sectional thrust increases with M_{tip} and exhibits greater fluctuation. Conversely, for identical M_{tip} values, the sectional thrust decreases with M_∞ due to a reduced angle of attack.

Refined Flow Conditions The impact of propeller speed on wing loading is depicted in Fig. 14 for the refined flow cases. There is a subtle increase in the suction peak with an increase in tip Mach number. For the average pressure on the advancing side, as shown in Fig. 14a, the pressure coefficient at the suction peak for the nominal condition is -1.08. In comparison, the pressure coefficient at the suction peak is -0.963 for M_{tip} =0.3 and -1.17 for M_{tip} =0.4. This indicates that the peak suction value becomes more responsive to changes in the

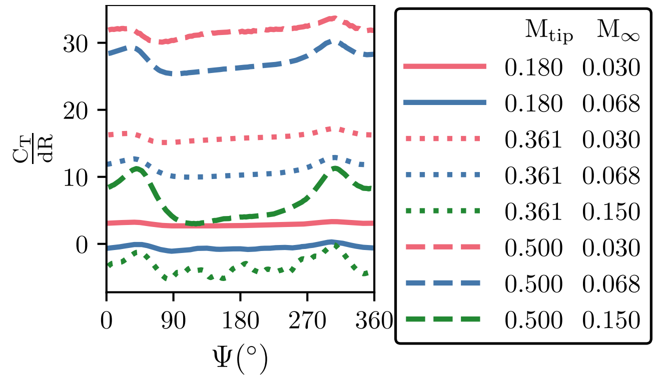

Fig. 13: Blade sectional thrust at $r = 0.75R$ over one revolution with freestream speed and rotor speed variations.

tip Mach number as the tip Mach number increases. Furthermore, Figures 14c and 14d illustrate that the unsteady pressure also increases with the propeller rotation rate, but with a more pronounced effect. The peak $C'_{p,\,RMS}$ values on the advancing side, aft of the leading edge, are 0.051, 0.109, and 0.155 for M_{tip} = 0.3, 0.361, and 0.4, respectively, showcasing the significant influence of propeller speed on the wing unsteady aerodynamic loading.

The impact of freestream velocity on wing loading is depicted in Fig. 15. As the freestream velocity increases, the average loading on the wing within the propeller slipstream decreases, with a more pronounced effect observed on the advancing side. Figure 12 showed that an increase in freestream velocity leads to a reduction in propeller thrust. This suggests that wing loading is affected by propeller thrust through changes in the induced velocity and dynamic pressure within the slipstream. The reduced induced velocity with the lower thrust leads to reduction in the overall incoming velocity toward the wing. Furthermore, an increased freestream velocity tends to stabilize the pressure distribution over the wing, leading to a reduction in $C'_{p,\,RMS}$, along with the reduced overall incoming velocity. This trend aligns with that of the average propeller thrust but contrasts with the trend observed for unsteady propeller thrust, indicating a complex interplay between freestream velocity, propeller thrust, and wing loading dynamics.

Aeroacoustic Results

Basic Flow Conditions Figure 16 shows the aeroacoustic directivity across eight flow conditions. The trends in aeroacoustic directivity exhibit dependence on both the freestream velocity and the tip Mach number. Notably, the null region at $\phi = 135^\circ$ is most pronounced for the baseline tip Mach number, especially at low and baseline airspeeds. For M_{tip} = 0.5 and M_∞ = 0.15, the null region occurs at a lower elevation angle and is less pronounced. Reducing the freestream Mach number to 58% below the baseline (M_∞ =0.030) shows a negligible effect on noise at a tip Mach number of 0.361, suggesting that the propeller's influence on noise is predominant when the advance ratio is low. However, at a tip Mach number

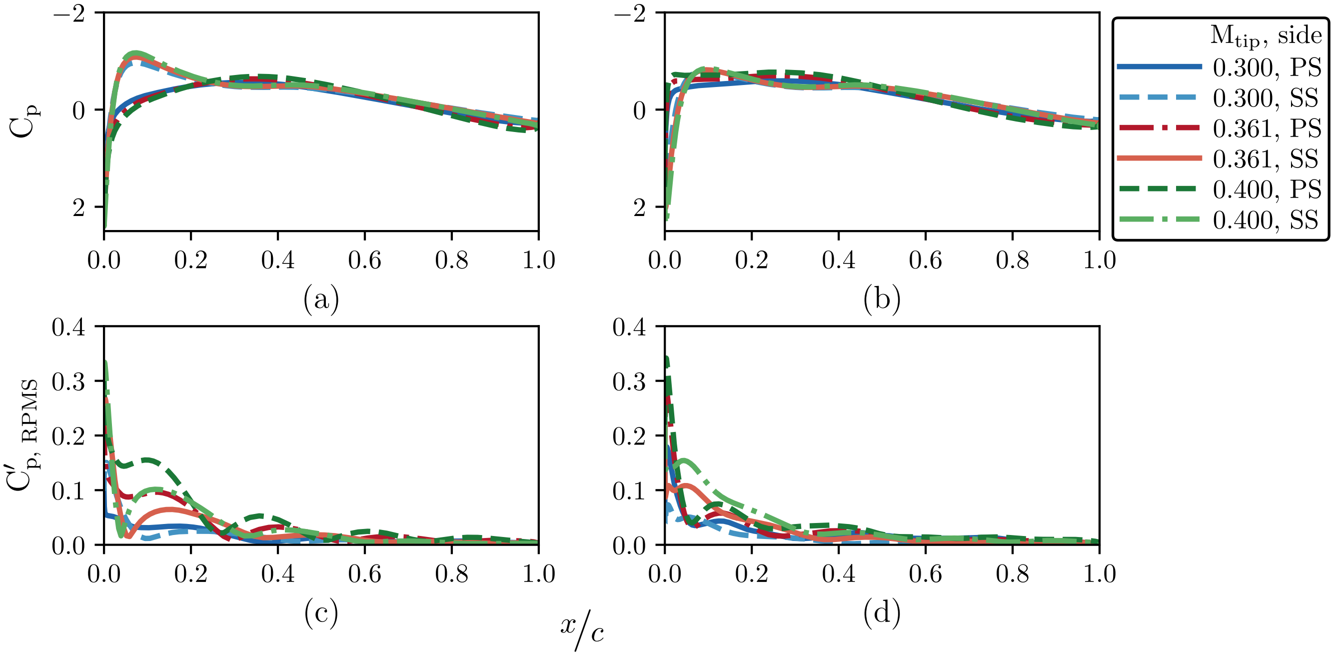

Fig. 14: Wing pressure prediction with variations of tip Mach number: (a) average pressure coefficient on the advancing side, (b) average pressure coefficient on the retreating side, (c) RMS of pressure coefficient on advancing side, and (d) RMS of pressure coefficient on the centerline.

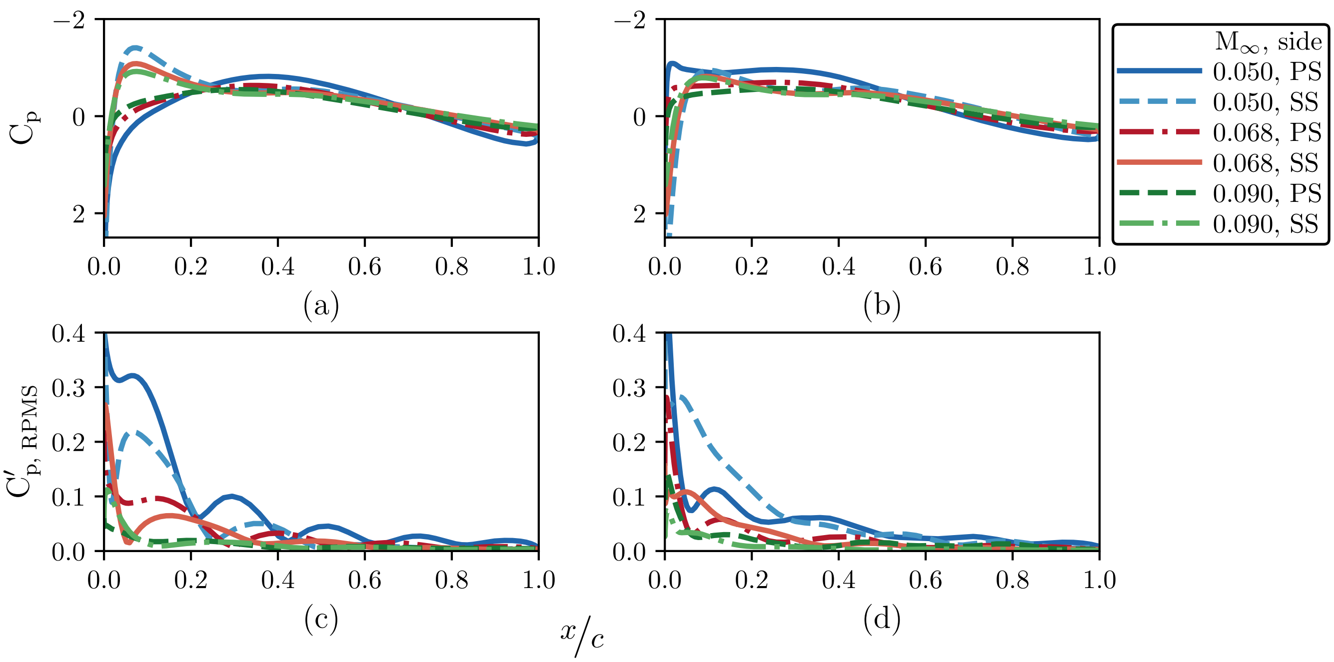

Fig. 15: Wing pressure prediction with variations of freestream Mach number: (a) average pressure coefficient on the advancing side, (b) average pressure coefficient on the retreating side, (c) RMS of pressure coefficient on advancing side, and (d) RMS of pressure coefficient on the centerline.

of 0.361 and a freestream Mach number of 0.068, it was observed that the acoustic pressure from the wing significantly exceeds that from the propeller, as noted by Trembois et al. (Ref. 6). This behavior could be attributed to the significant impact of propeller wash on wing noise. Moreover, the overall acoustic results show a marked sensitivity to changes in tip Mach number. Halving the tip Mach number from its baseline value leads to a reduction in tonal noise by over 10 dB across almost all elevation angles, excluding the null region. Conversely, increasing the tip Mach number to 0.5 results in a significant deviation, with more than 20 dB increase in the rotor plane, underscoring the critical role of rotational speed in determining the acoustic profile and highlighting its significance for noise mitigation in various operational scenarios. Apart from the null regions, an increase in freestream velocity leads to a more uniform SPL across all elevation angles, thereby diminishing the effects of directivity.

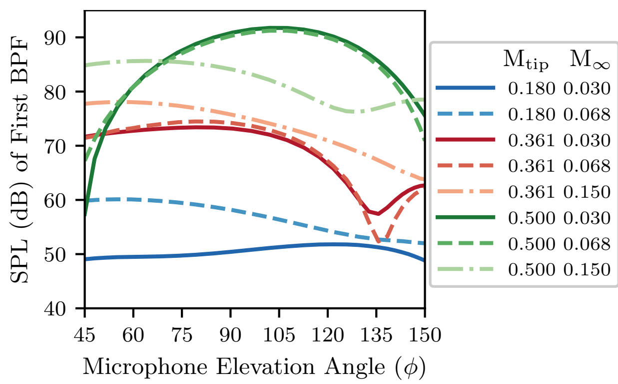

Fig. 16: A comparison of the directivity operating in various flow conditions.

Figure 17 illustrates the sensitivity of the first BPF to flow speed and propeller rotation rate for an observer at $\phi = 90.61°$. For the baseline tip Mach number, the acoustic predictions show minimal sensitivity to freestream velocity; the SPL values of the first BPF are all within a 2.5 dB range. However, the range of SPL is 7.69 dB for the low tip Mach number and 6.93 dB for the high tip Mach number. For the lower propeller rotation rate, increasing the freestream Mach number increases noise, while increasing the freestream Mach number for the higher tip Mach number decreases the noise. For lower thrust, the total noise is more dependent on the wing contribution, thus the freestream Mach number. However, even at the higher tip Mach number, the increased freestream Mach number reduces the propeller thrust and its contribution to the noise. The SPL at the reduced airspeed maintains consistent sensitivity to tip Mach number within the range simulated. Meanwhile, the SPL at the nominal airspeed becomes more sensitive to tip Mach number as tip Mach number increases. The nominal and reduced airspeed simulations are within 1.01 dB for the nominal and increased tip Mach number. On the other hand, the SPL at the increased airspeed is greatest at the baseline tip Mach number but becomes the lowest at increased tip Mach number. This possibly indicates that when the advance ratio is low enough, the noise is insensitive to changes in freestream Mach number.

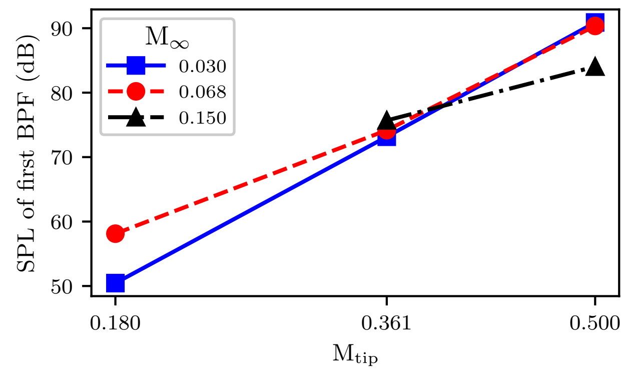

Fig. 17: A comparison of the first blade passing frequency directly below the propeller ($\phi = 90.61°$).

Refined Flow Conditions Figure 18 illustrates the acoustic contributions from both the propeller and wing, alongside the total acoustic levels, under the refined flow conditions observed at a single observer location ($\phi = 90.61°$). Each plot employs a consistent color scale for direct comparison, whereas the isolines are individually scaled to highlight source-specific trends. The points mark the locations from which the simulation data are derived, with the intervening values being interpolated. The range of SPL for the first BPF within the refined flow condition set ranges from 52.5 dB to 77.5 dB for the propeller, and from 54 dB to 74 dB for the wing. Figure 18a reveals that the first BPF of the propeller reacts to variations in both the tip and freestream Mach numbers within the specified refined condition range. Disregarding the outlier at $M_{tip} = 0.25$ and $M_\infty = 0.09$, the SPL undergoes an average change of (+1.33 dB)/(0.01 M_{tip}) and (-1.61 dB)/(0.01 M_∞). Figure 18b shows that the SPL for the first BPF of the wing becomes increasingly sensitive to the tip Mach number as the freestream Mach number rises. This highlights the significant impact of the propeller wake on unsteady wing loading, a key factor in wing acoustics. Figure 18c presents the first BPF of the overall noise. While both the propeller and wing are influenced by M_∞ at higher M_{tip} values, the resulting trends are contrary, leading to a minimal dependence on M_∞ at elevated M_{tip} levels for the aggregate noise. The variation in total noise across the freestream Mach number range at a nominal M_{tip} is less than 2 dB, which is consistent with Fig. 17

Figure 19 displays the difference in acoustic contributions between the propeller and the wing. At the lowest freestream speeds and highest rotation rates, the propeller emits a SPL that is 7 dB higher than that of the wing. In contrast, at the highest freestream speeds and lowest rotation rates, a condition where the wing's acoustic output prevails, the wing produces an SPL 3 dB higher than the propeller's. The wing emerges as the principal source of noise when the freestream Mach number exceeds 0.06 and the tip Mach number falls below 0.3, corresponding to advance ratios greater than 0.628.

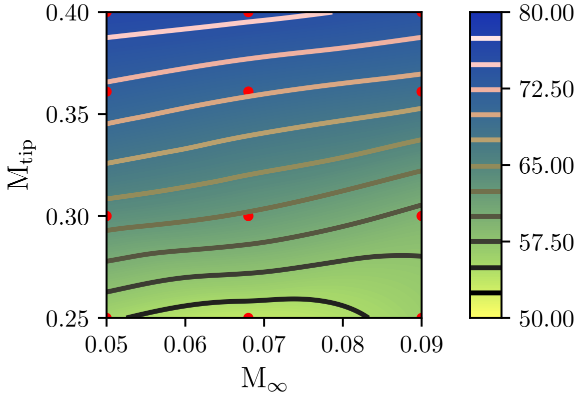

(a) Propeller

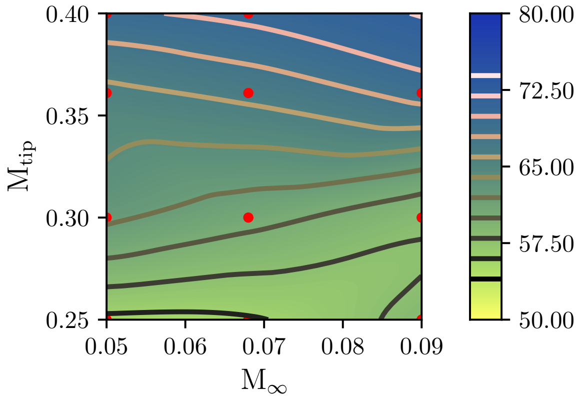

(b) Wing

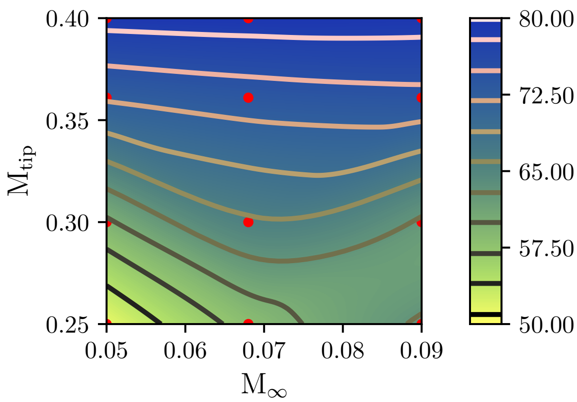

(c) Total

Fig. 18: Variation of the SPL for the first BPF directly below the propeller ($\phi = 90.61°$).

Moreover, as the RPM increases, the impact of the freestream speed on the dominance of propeller noise becomes more pronounced.

Angle of Attack Effect

Aerodynamic Results The steady and unsteady wing loadings are depicted in Fig. 20 across all simulated angles of attack. Trends in the average pressure coefficient remain consistent between the advancing and retreating sides of the wing. The wing's pressure coefficient, averaged over one revolution, shows greater sensitivity to changes in the wing's angle of attack than to changes in the propeller's angle of attack. Table 2 presents the pressure coefficient C_p at the suction peak for each tested condition. An increase in the propeller's angle of attack alone reduces the suction peak by 12%, while an increase solely in the wing's angle of attack enhances the suction peak by 69%. The predicted suction peak for both surfaces at a given angle of attack is 4.9% lower than that for the wing alone at the same angle of attack. The propeller's angle of attack relative to the wing introduces a negative effective angle of attack through the downwash slipstream, thereby influencing the wing loading with the reduced suction peak.

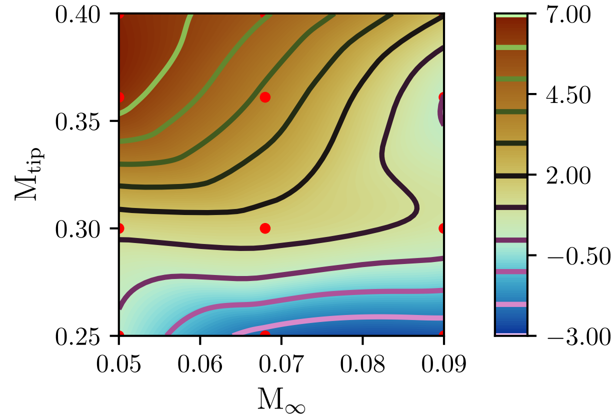

Fig. 19: The difference of SPL in dB for the first BPF of the propeller and wing surfaces directly below the propeller.

Table 2: Coefficient of pressure suction peak for each angle of attack.

$\alpha_w(°)$	$\alpha_p(°)$	C_p
0	0	−1.08
0	5	−0.948
5	0	−1.83
5	5	−1.74

The unsteady wing pressure, subject to variations in the angle of attack, is illustrated in Figs. 20c and 20d. When the wing alone is inclined, the unsteady pressure magnitude on the pressure side of the wing—within the advancing blade tip vortex trajectory, as shown in Fig. 20c—increases from the baseline condition. Conversely, the peak $C'_{p,RMS}$ resulting from the tip vortex interacting with the pressure side of the wing diminishes compared to the baseline condition when only the propeller is inclined. The variations in unsteady pressure predominantly stem from the differences in the propeller and wing angles of attack. The smallest discrepancies between conditions occur when the propeller and wing share the same angle of attack ($\alpha_p = 0°, \alpha_w = 0°$ and $\alpha_p = 5°, \alpha_w = 5°$). In the scenario where $\alpha_p = 5°$ and $\alpha_w = 0°$, Fig. 20d indicates

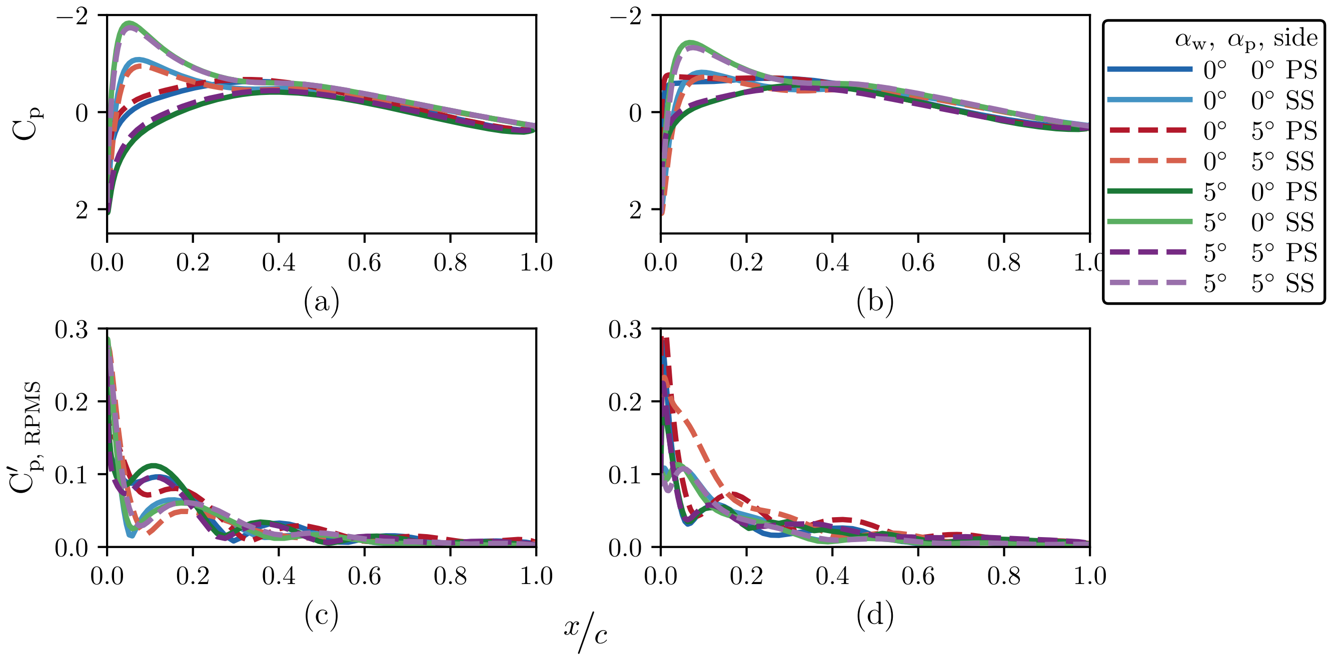

Fig. 20: Wing pressure with variations of angles of attack: (a) average pressure coefficient on the advancing side, (b) average pressure coefficient on the retreating side, (c) RMS of pressure coefficient on advancing side, and (d) RMS of pressure coefficient on the centerline.

that $C'_{p,\,RMS}$ on the suction side of the centerline remains pronounced further downstream compared to other conditions. This effect is attributed to the propeller's angle of attack bringing the propeller tip closer to the wing's leading edge and causing the slipstream to interact with the wing surface at an oblique angle. Similarly, with the wing inclined relative to the propeller, $C'_{p,\,RMS}$ on the pressure side increases along the centerline, highlighting the complex interplay between wing and propeller angles in influencing unsteady aerodynamic pressures.

The propeller loading with variations in angle of attack are shown in Fig. 21. Figure 21a illustrates that elevations in both the wing and propeller angles of attack lead to an increase in the average thrust over one revolution. Within the simulated range of angles of attack, the propeller's angle of attack has a lesser impact on the propeller thrust compared to the wing's angle of attack. This suggests the significant influence of wing thickness and loading on propeller thrust. Despite the velocity variation across the propeller disk induced by the propeller's angle of attack, there is a decrease in the total propeller thrust harmonics as shown in Fig. 21b.

Figure 22 presents the loading of individual blades over one revolution at 75% of the radius. Interestingly, while the total thrust harmonics are at their lowest when only the propeller is inclined, the condition also results in the largest peak-to-peak blade loading along the azimuthal angle. This phenomenon is attributed to the blade that transitions from the pressure side to the suction side of the wing, experiencing reduced tangential velocity when the propeller is inclined. Consequently, this leads to a diminished thrust near $\psi = 270°$ for $\alpha_p = 5°$. Conversely, the blade moving from the suction side to the pressure side, around $\psi = 90.61°$, experiences an increase in tangential velocity due to the propeller's angle of attack, resulting in enhanced thrust generation. With an increase in the wing's angle of attack, both the wing loading and circulation rise, leading to a stronger downwash effect on the propeller. This intensified downwash contributes to a more pronounced thrust deficit near $\psi = 0°$.

Aeroacoustic Results The first BPF of the total SPL measured at a linear array of observers, as depicted in Fig. 23, is lowest under the nominal condition or zero angles of attack. The SPL is greatest when the propeller is incline for the full range of directivity. For elevation angles ranging from 80° to 120°, noise levels are highest when both the wing and propeller are inclined. Outside this angular span, acoustic levels are more pronounced when only the propeller is inclined. The positioning of the propeller and wing becomes closer to the microphone at $\phi = 90.61°$ for $\alpha_w = 5°$ and $\alpha_p = 5°$ due to the orientation of their angles of attack. This proximity difference diminishes at lower and higher elevation angles. The trends in directivity are further complicated by the interference between the acoustic signals from the propeller and wing. Notably, a noise reduction near $\phi = 135°$ results from destructive interference between these sources. Moreover, with $\alpha_w = 0°$ and $\alpha_p = 5°$, the reduced distance between the propeller plane and the wing leading edge alters the phase offset and interference pattern.

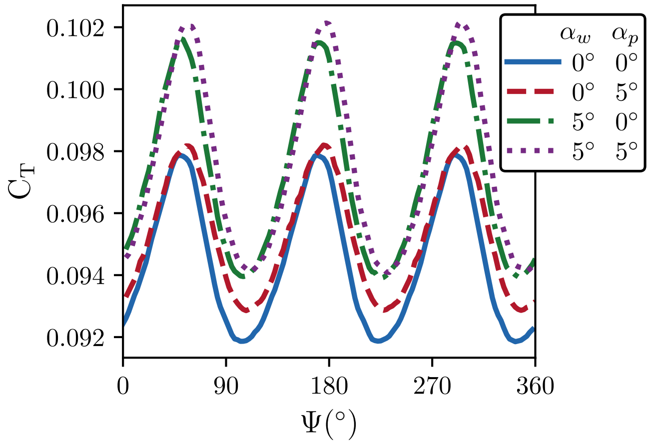

(a)

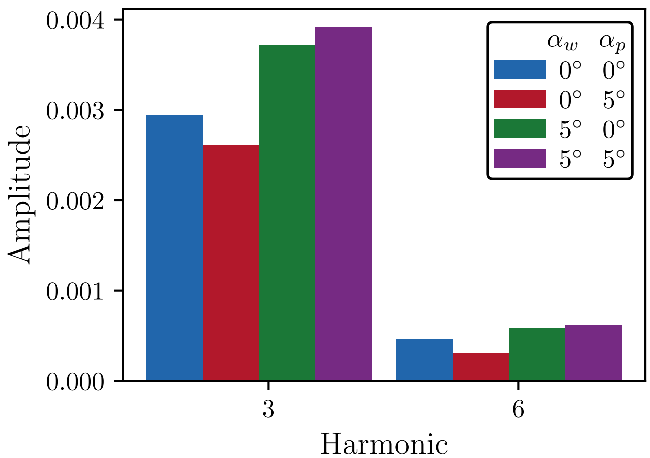

(b)

Fig. 21: Total propeller thrust with angle of attack variation: (a) throughout one revolution and (b) harmonics during one revolution.

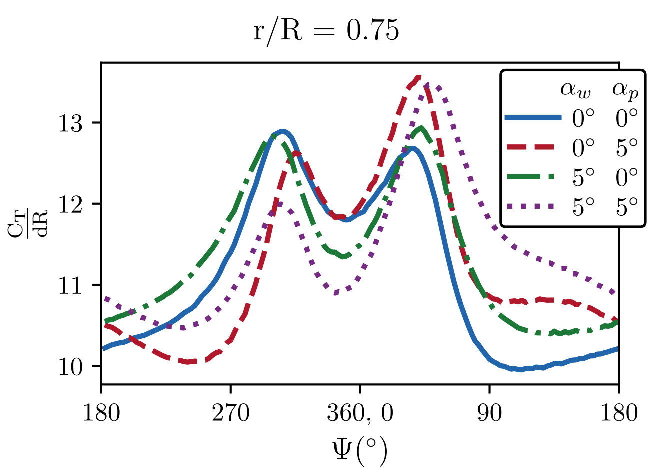

Fig. 22: Blade sectional thrust at r = 0.75R over one revolution with angle of attack variation.

Figure 24 displays the acoustic contributions at a single observer location ($\phi = 90.61°$), highlighting the sensitivity of the wing's loading noise to variations in the angles of attack for both the propeller and wing. The wing loading noise fluctuates between 66.7 dB and 75.8 dB across different conditions, demonstrating a broad sensitivity to changes in the angle of attack. In contrast, adjustments to the angle of attack lead to an increase in propeller noise from the baseline condition by up to 2.15 dB, with the maximum increase occurring when $\alpha_w = 0°$ and $\alpha_p = 5°$. This indicates that the propeller noise is more responsive to changes in the propeller's angle of attack than to variations in the wing's angle, aligning with observations of unsteady propeller blade loading as depicted in Fig. 22. Furthermore, the SPL of the first BPF from the wing reaches its peak for $\alpha_w = 0°$ and $\alpha_p = 5°$. This is in line with the highest $C'_{p,\,\mathrm{RPM}}$ values at the propeller centerline, as shown in Fig. 20d.

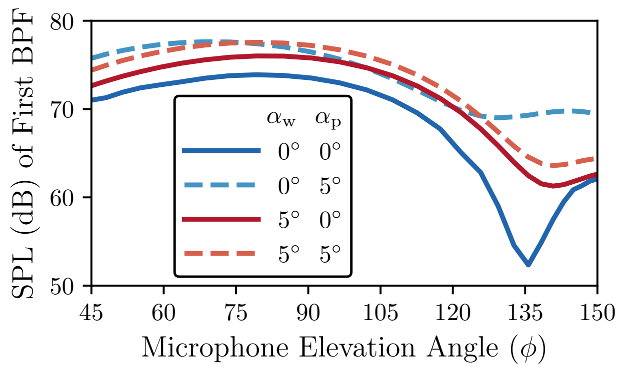

Fig. 23: Acoustic directivity with variations in propeller and wing angle of attack at a single wing position.

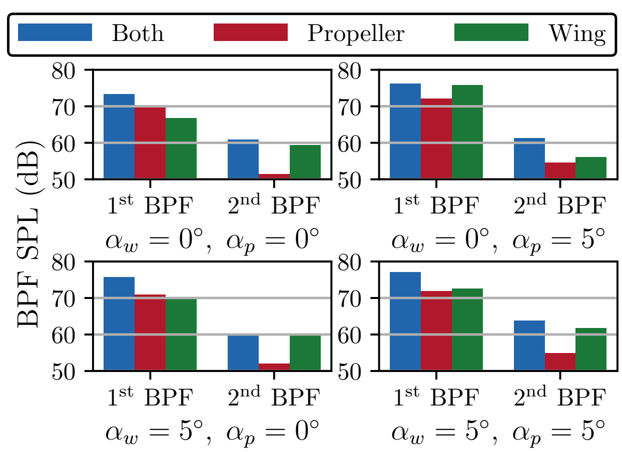

Fig. 24: SPL of the first two BPFs observed at $\phi = 90.61°$ with variations in propeller and wing angle of attack.

Side Slip Angle Effect

Aerodynamic Results The propeller thrust dependence on side slip angle is shown in Fig. 25. Figure 25a illustrates that an increase in side slip angle results in heightened thrust, aligning with the observed trend where a reduction in freestream Mach number leads to an increase in thrust. This increase in thrust can be attributed to the augmentation in the freestream velocity normal to the propeller plane and a decrease in the advance ratio as the side slip angle increases. Further, Fig. 25b reveals that the total loading harmonics decrease as the side slip angle grows.

Contrary to the overall propeller loading, the unsteady blade loading, as depicted in Fig. 26, intensifies with the side slip angle. Specifically, blade azimuths ranging from $\psi = 270^\circ$ through $\psi = 90.61^\circ$ exhibit an increase in tangential velocity due to the side slip angle, whereas azimuths from $\psi = 90.61^\circ$ to $\psi = 270^\circ$ experience a decrease in tangential velocity. This variation in velocity correlates directly with the observed regions of increased and decreased thrust on the blades relative to the nominal condition. In the nominal condition, the peak thrust occurring as the blade transitions from the suction side to the pressure side of the wing is less than the peak thrust experienced as the blade moves from the pressure side to the suction side. However, with an increase in side slip angle, the situation reverses; the thrust peak on the advancing blade (around $\psi \approx 45^\circ$) exceeds that of the blade on the retreating side (around $\psi \approx 315^\circ$). This shift in thrust peaks can also be attributed to the increased tangential velocity due to the side slip.

Aeroacoustic Results Figure 27 demonstrates the SPL for the first BPF across various side slip angles, revealing a uniform directivity pattern up to $\phi = 120^\circ$. Beyond this elevation angle, phasing influences that are not directly related to the noise source physics begin to modify the observed trends. Across the entire spectrum of observer locations, the SPL trends upwards with an increase in side slip angle. Notably, up to $\phi = 110^\circ$, the SPLs for all side slip angles remain within 5% of the nominal condition, indicating a relatively minor impact of side slip on SPL within this range. Specifically, the discrepancy between the SPLs for the five and ten degree side slip angles is even more negligible, staying within 1% of each other up to $\phi = 110^\circ$. This close correspondence suggests that the aerodynamic and acoustic impacts of side slip angles within this range are subtle yet measurable. The skewing of the slipstream by the side slip angle, which plays a crucial role in generating unsteady loading over the wing, shifts the concentration of wing loading. Consequently, this alters the phase relationship between the propeller and wing noise sources, leading to a reduction in destructive interference at $\phi = 135^\circ$. This phase shift effectively diminishes the cancellation effects that typically lower SPLs, resulting in the observed increase in noise levels.

CONCLUSIONS

The interaction aerodynamics and aeroacoustics between a Mejzlik 16x11 propeller and a wing with NACA 63_2-215 MOD B airfoil sections were analyzed under varied conditions: freestream velocity, propeller tip Mach number, angle of attack, and side slip angle. This study aimed to elucidate

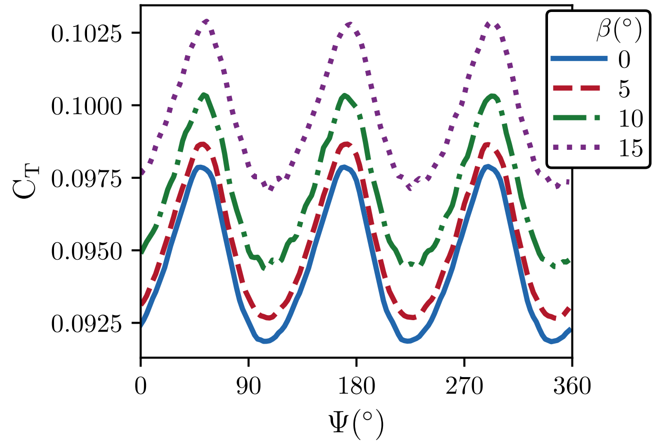

(a)

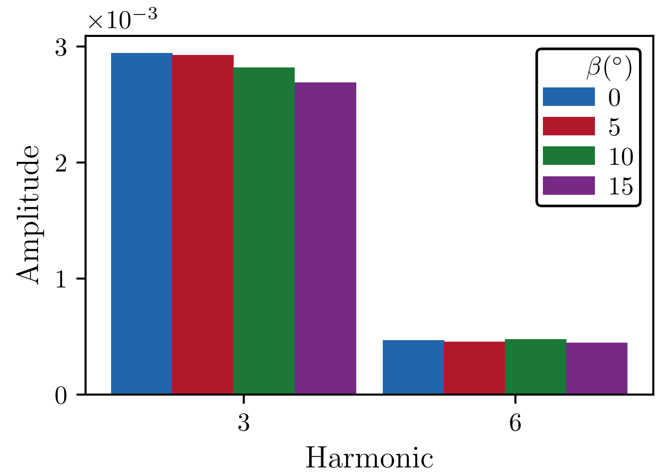

(b)

Fig. 25: Total propeller thrust over one revolution with side slip angle variation: (a) azimuthal dependence, (b) harmonics of the first two BPFs.

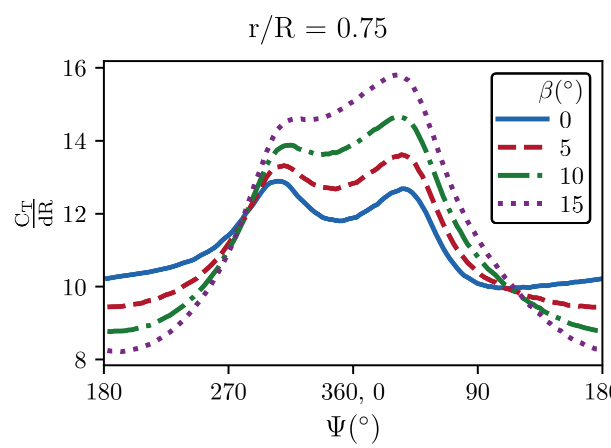

Fig. 26: Blade sectional thrust at $r = 0.75R$ over one revolution with side slip angle variation.

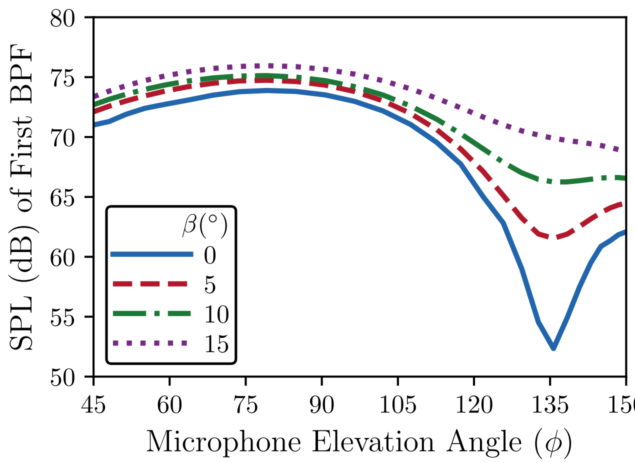

Fig. 27: Acoustic directivity with variations in side slip angle.

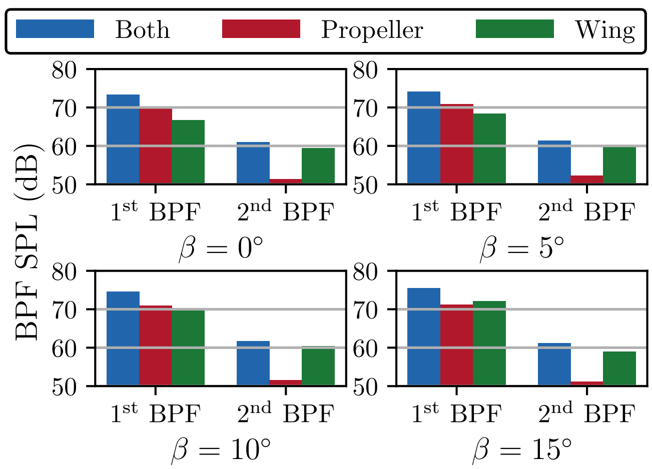

Fig. 28: SPL of the first two BPFs observed at $\phi = 90.61°$ with variations in side slip angle.

the effects of these parameters on both aerodynamic performance and acoustic properties. An increase in freestream Mach number led to a higher advance ratio which diminished the average propeller thrust, but increased thrust harmonics. Conversely, elevations in tip Mach number enhanced both the average propeller thrust and thrust harmonics. The steady and unsteady wing loading exhibited a positive correlation with tip Mach number, contrasting with their negative relationship with freestream Mach number. Regarding aeroacoustics, the propeller's noise decreased with an increase in M_∞, despite the propeller thrust harmonics showing an upward trend with M_∞. The wing's aeroacoustic sensitivity to M_{tip} intensified as M_∞ increased. Notably, the propeller produced more noise than the wing at the first BPF when $M_{\text{tip}} > 0.3$. The overall aeroacoustic outcome, influenced by the combined noise emissions from both the propeller and wing, was significantly affected by destructive interference, which varied according to flow conditions and observer location. This interference complicated the direct linkage of observed trends to specific physical mechanisms. Such findings highlight the complex dynamics between aerodynamic forces and aeroacoustic emissions under various operational conditions, emphasizing the intricate balance needed for optimal performance and noise reduction in propeller-wing configurations.

The wing angle of attack exerts a more significant influence on both the wing loading and the average propeller loading compared to the propeller angle of attack. With an increase in the wing angle of attack, the effect on wing loading intensifies, leading to an augmentation in propeller thrust. This suggests a synergistic interaction where aerodynamic adjustments to the wing can enhance the propulsion efficiency of the system. The overall aeroacoustic behavior tends to mirror the sensitivity pattern of the wing, demonstrating a higher responsiveness to changes in the wing's angle of attack than to variations in the propeller's angle. This heightened sensitivity of the wing to aerodynamic adjustments is further evidenced by the range of the first BPF of wing SPL, which was observed to be four times greater for all angles of attack than that attributed to the propeller. This disparity in sensitivity highlights the critical role of wing geometry and orientation in influencing both the aerodynamic performance and aeroacoustic characteristics of the aircraft. The findings underscore the importance of optimizing the wing's angle of attack to achieve desirable performance outcomes, both in terms of thrust efficiency and noise mitigation.

The side slip angle distorts the propeller wake, resulting in an increase in thrust for the advancing blade and a reduction in thrust deficit caused by wing downwash. This adjustment in the wake's directionality not only optimizes the propeller's efficiency but also mitigates some of the adverse aerodynamic interactions between the propeller and wing. Acoustically, the trends are consistent and monotonic for the first BPF of the SPL for both surfaces, as well as for the total noise observed. As the side slip angle increases, there is a corresponding rise in SPL, with the wing experiencing a more pronounced effect. This suggests that the side slip angle not only influences the aerodynamic performance of the aircraft but also significantly affects its aeroacoustic behavior. The greater impact on wing acoustics can be attributed to the altered flow field around the wing due to side slip. These findings underscore the intricate relationship between aircraft orientation, aerodynamic forces, and aeroacoustic emissions, highlighting the need for careful consideration of side slip angles in the design and operation of aircraft to balance performance with noise reduction.

ACKNOWLEDGMENTS

This research is partially funded by the Government under Cooperative Agreement No. W911W6-21-2-0002. The U.S. Government is authorized to reproduce and distribute reprints for Government purposes notwithstanding any copyright notation thereon. The views and conclusions contained in this document are those of the authors and should not be interpreted as representing the official policies or position, either expressed or implied, of the U.S. Army Combat Capabilities Development Command (DEVCOM), Aviation & Missile

Center (AvMC), or the U.S. Government. Resources supporting this work were provided by the NASA High-End Computing (HEC) Program through the NASA Advanced Supercomputing (NAS) Division at Ames Research Center.

REFERENCES

[1]Lim, J. W., "Fundamental Investigation of Proprotor and Wing Interactions in Tiltrotor Aircraft," Proceedings of the 75th Annual Forum of the Vertical Flight Society, Philadelphia, Pennsylvania, May 13–16, 2019.

[2]Zhang, J., Brentner, K. S., and Smith, E. C., "Prediction of the Aerodynamic and Acoustic Impact of Propeller-Wing Interference," Proceedings of the Vertical Flight Society Technical Conference on Aeromechanics Design for Transformative Vertical Flight, San Jose, California, May 21–23, 2020.

[3]Stephenson, J. H., Schatzman, N. L., Cheung, B. K., Zawodny, N. S., Sargent, D. C., and Sim, B. W.-C., "Aeroacoustic Measurements from the Aerodynamic and Acoustic Rotorprop Test (AART) in the National Full-Scale Aerodynamics Complex (NFAC) 40- by 80-Foot Wind Tunnel," Proceedings of the 77th Annual Forum of the Vertical Flight Society, Virtual, May 10–14, 2021.

[4]Jia, Z., Lim, J., and Jain, R., "Computational Study on the Aerodynamic and Acoustic Rotorprop Test in the NFAC 40- by 80-Foot Wind Tunnel," Proceedings of the 79th Annual Forum of the Vertical Flight Society, West Palm Beach, Florida, May 16–18, 2023.

[5]Zawodny, N. S., Boyd, D. D., and Nark, D. M., "Aerodynamic and Acoustic Interactions Associated with Inboard Propeller-Wing Configurations," Proceedings of the AIAA Scitech Forum, Virtual, January 19–21, 2021, AIAA Paper 2021-0714.

[6]Trembois, N., Brown, E., Lee, S., Ramsarran, T., and Brentner, K. S., "Prediction of Interactional Aerodynamic Noise of Propellers and Wing Using High-Fidelity CFD," Proceedings of the 79th VFS Forum, West Palm Beach, Florida, May 16–18, 2023.

[7]Ramsarran, T., Brentner, K. S., Trembois, N., Brown, E., and Lee, S., "Evaluating Propeller-Wing Interactional Noise Predictions from a Medium-Fidelity Approach," Proceedings of the 6th Decennial VFS Aeromechanics Specialists' Conference, Santa Clara, California, February 6–8, 2024.

[8]Draper, J. W. and Kuhn, R. E., "Investigation of the Aerodynamic Characteristics of a Model Wing-Propeller Combination and of the Wing and Propeller Separately at Angles of Attack up to 90°," NACA TN 3304, 1954.

[9]Quackenbush, T. R., Wachspress, D. A., Yu, M. K., and Solomon, C. L., "Modeling of Proprotor/Wing/Flap Interaction for Advanced Vertical Lift Aircraft," Proceedings of the 76th Annual Forum of the Vertical Flight Society, Virtual, October 5–8, 2020.

[10]Brown, E., Trembois, N., Lee, S., Ramsarran, T., and Brentner, K. S., "Effect of Flaps on Propeller and Wing Aerodynamics and Acoustics using Computational Fluid Dynamics and Viscous Vortex Particle Method," Proceedings of the AIAA Aviation Forum, Las Vegas, Nevada, July 29–August 2, 2024.

[11]Jia, Z., Lee, S., Sharma, K., and Brentner, K. S., "Aeroacoustic Analysis of a Lift-Offset Coaxial Rotor Using High-Fidelity CFD/CSD Loose Coupling Simulation," *Journal of the American Helicopter Society*, Vol. 65, (012011), 2020, pp. 1–15.

[12]Jia, Z. and Lee, S., "Computational Study on Noise of Urban Air Mobility Quadrotor Aircraft," *Journal of the American Helicopter Society*, Vol. 67, 2022, pp. 012009.

[13]Jia, Z. and Lee, S., "High-Fidelity Computational Analysis on the Noise of a Side-by-Side Hybrid VTOL Aircraft," *Journal of the American Helicopter Society*, Vol. 67, 2022, pp. 022005.

[14]Sagaga, J. and Lee, S., "Performance, Aerodynamics, and Aeroacoustics of Side-by-Side Rotors Using High-Fidelity Computational Fluid Dynamics," *AIAA Journal*, Vol. 61, (12), 2023, pp. 5429–5445.

[15]Li, S. and Lee, S., "Prediction of Rotorcraft Broadband Trailing-Edge Noise and Parameter Sensitivity Study," *Journal of the American Helicopter Society*, Vol. 65, 2020, pp. 042006.

[16]Li, S. and Lee, S., "Prediction of Urban Air Mobility Multirotor VTOL Broadband Noise Using UCD-QuietFly," *Journal of the American Helicopter Society*, Vol. 66, 2021, pp. 032004.

[17]Trembois, N. P., *Automatic Mesh Generation of Structured Overset Rotor Blades*, Master's thesis, University of California, Davis, Davis, CA, December 2020.

[18]Nichols, R. and Buning, P., *User's Manual for OVERFLOW 2.2*, NASA Langley Research Center, Hampton, Virginia, August 2010.

[19]Nichols, R., Tramel, R., and Buning, P., "Solver and Turbulence Model Upgrades to OVERFLOW 2 for Unsteady and High-Speed Flow Applications," Proceedings of the 25th AIAA Applied Aerodynamics Conference, San Fransisco, California, June 5–8, 2006, AIAA Paper 2006-2824.

[20]Brès, G., *Modeling the Noise of Arbitrary Maneuvering Rotorcraft: Analysis and Implementation of the PSU-WOPWOP Noise Prediction Code*, Master's thesis, The Pennsylvania State University, University Park, Pennsylvania, June 2002.

[21]Brentner, K. S., Bres, G. A., Perez, G., and Jones, H. E., "Maneuvering rotorcraft noise prediction: a new code for a new problem," American Helicopter Society Aerodynamics, Acoustics, and Test and Evaluation Technical Specialist Meeting, Jan 23–25 2002.

[22]Brès, G. A., Brentner, K. S., Perez, G., and Jones, H. E., "Maneuvering rotorcraft noise prediction," *Journal of Sound and Vibration*, Vol. 275, (3–5), August 2004, pp. 719–738. doi: https://doi.org/10.1016/j.jsv.2003.07.005

[23]Lee, S., Brentner, K., Farassat, F., and Morris, P., "Analytic formulation and numerical implementation of an acoustic pressure gradient prediction," *Journal of Sound and Vibration*, Vol. 319, (3-5), 2009, pp. 1200–1221.

[24]Ffowcs, W. and Hawkings, D. L., "Sound Generation by Turbulence and Surfaces in Arbitrary Motion," *Philos. Trans. R. Soc. A*, Vol. 264, (1151), 1969, pp. 321–342.

[25]Farassat, F. and Succi, G., "The Prediction of Helicopter Discrete Frequency Noise," *Vertica*, June 1983, pp. 309–320.

APPENDIX

Directivity Null Region

The acoustic directivity observed in Figs. 7–9 and 11 reveals a region at high elevation angles where the noise is significantly reduced or nullified. Specifically, the acoustic pressure at two elevation angles ($\phi = 90.61°$ and $135°$) is detailed in Fig. 29 for $M_\infty = 0.068$ and $M_{tip} = 0.361$. While directivity and the varying distances from the propeller and wing surfaces to the observers, as indicated by the propeller thickness noise, do influence the reduced acoustic pressure at higher elevation angles, they alone do not fully account for the observed null region. Fig. 29b demonstrates that the acoustic pressures from the propeller and wing loading are almost completely out of phase at $\phi = 135°$. Consequently, the amplitude of the total noise is lower than that of either loading noise source alone. The total noise's acoustic pressure signal at the first BPF aligns with the propeller thickness acoustic pressure, while the pattern of the higher harmonics follows that of the wing loading noise. This intricate interplay between propeller and wing noise, especially at specific angles like 135°, highlights the complex nature of acoustic directivity and its dependence on phase relationships between different noise sources. Interestingly, the experimental data do not exhibit this null region at this specific observer location. It is possible that acoustic scattering by the test structure might play a role in mitigating the phase cancellation effect. Further studies are needed to investigate and verify this discrepancy.

Figure 30 highlights the differences in SPL at the first two BPFs for the propeller and wing loading at $\phi = 50°, 90.61°$, and $\phi = 135°$. For Fig. , the total noise is lower than the individual sources for the first two BPFs, indicating that destructive interference significantly affects total noise, with its effect being highly dependent on the observer location. The first BPF of the propeller and wing exhibit similar magnitudes, at 64.2 dB and 64.9 dB, respectively. This similar magnitude exacerbates the phase cancellation, as the signals can sum to nearly zero when there is a perfect phase offset. This phase cancellation does not appear at $\phi = 50°$ and $90.61°$.

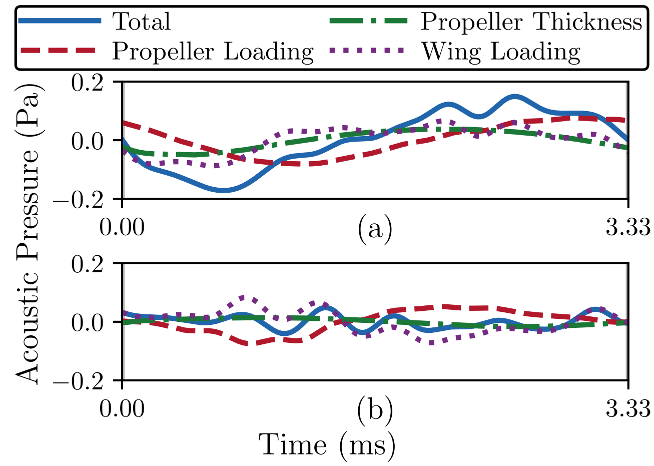

Fig. 29: A comparison of the acoustic pressure for the nominal condition for one-third of a revolution: (a) $\phi = 90.61°$, (b) $\phi = 135°$.

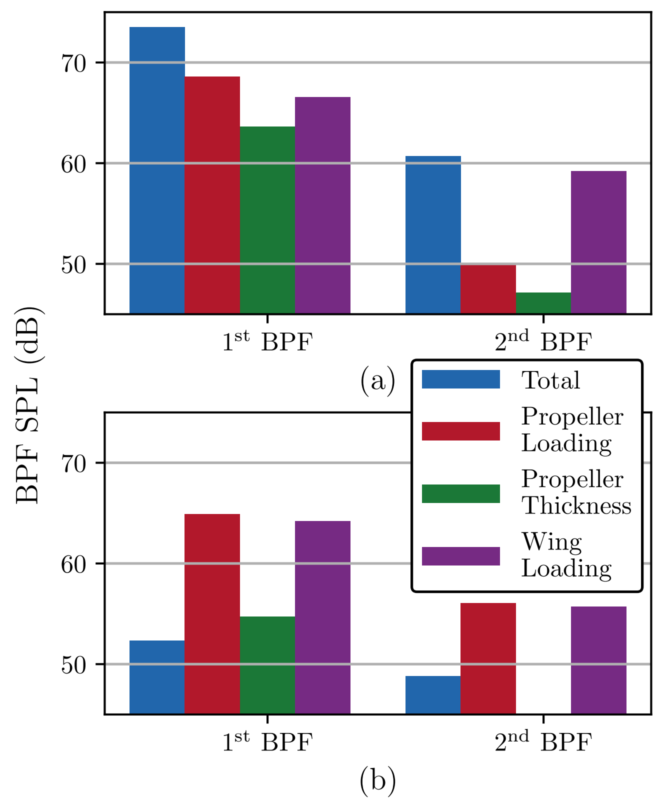

Fig. 30: A comparison of the acoustic spectrum for the nominal condition: (a) $\phi = 90.61°$, (b) $\phi = 135°$.